Postmidnight storm-time enhancement of tens-of-keV proton flux

Y. Ebihara[1]

Universities Space Research Association, NASA Goddard Space Flight Center, Greenbelt, Maryland, USA

M.-C. Fok

NASA Goddard Space Flight Center, Greenbelt, Maryland, USA

[1]   We investigated the global morphology of the storm-time distribution of ring current protons and energetic neutral atoms (ENAs) observed by the High-Energy Neutral Atom (HENA) imager on the IMAGE satellite. The postmidnight enhancements of the proton and ENA fluxes were in particular focused on in this study, and the following six possible mechanisms causing the postmidnight enhancements were tested by using a self-consistent kinetic simulation of the ring current protons: (1) shielding electric field, (2) gap between the region 2 field-aligned current and the auroral oval, (3) strong gradient of the ionospheric conductivity near the terminator, (4) plasma sheet density, (5) plasma sheet temperature, and (6) local-time dependence of the plasma sheet density. When the ring current is self-consistently coupled with the ionosphere through the region 2 field-aligned current, the simulated postmidnight enhancements are found to agree well with the IMAGE/HENA observations, even though effects other than shielding fields were not included. The overall convection strength is found to have a substantial influence on the morphology of the distribution of the ring current protons. The MLT of the flux peak is also shown to depend slightly on the plasma sheet density and solar activity. A local-time dependence of the plasma sheet density can produce a pronounced postmidnight enhancement without introducing the self-consistent electric field. Other possible mechanisms causing the postmidnight enhancements are also discussed in detail.   INDEX TERMS: 2778 Magnetospheric Physics: Ring current; 2740 Magnetospheric Physics: Magnetospheric configuration and dynamics; 2463 Ionosphere: Plasma convection; 2730 Magnetospheric Physics: Magnetosphere—inner; KEYWORDS: magnetic storms, energetic ions, energetic neutral atoms

1. Introduction

[2]   As revealed by the High-Energy Neutral Atom (HENA) imager [Mitchell et al., 2000] on board the IMAGE satellite [Burch, 2000], global emissions of tens-of-keV energetic neutral atoms (ENAs) exhibit a substantial enhancement in the postmidnight sector in the inner magnetosphere during the main phase of intense magnetic storms [C:son Brandt et al., 2002b]. The postmidnight enhancement of the tens-of-keV ENA emission probably reflects the fact that during the intense magnetic storms tens-of-keV ion flux is greatly enhanced in the postmidnight sector. Since a premidnight enhancement of the ion flux had been thought in a traditional wisdom (c.f. section 2), this new finding implies that the storm-time dynamics of the energetic ions in the inner magnetosphere is much more

complicated than thought before and challenges the conventional wisdom of premidnight enhancements of storm-time ring current.

[3]   So far, in situ satellite observations have shown that a majority of the storm-time enhancement of the tens-of-keV ion flux is in the premidnight sector. Stüdemann et al. [1987] have shown that during the 2–3 May 1986 storm (Dst minimum of −79 nT), the proton flux with 10–206 keV/q measured by the Viking satellite dramatically increased on the duskside (∼1800 MLT), while the proton spectrum was very similar to the quiet-time one on the dawnside (∼0600 MLT). Similarly, during the main phase of the 10–11 April 1997 storm (Dst minimum of −82 nT), a significant increase in the ion flux in the 30–80 keV energy range was also observed on the duskside (∼2000 MLT) by NOAA 12, while the flux remains almost steady on the dawnside (∼0800 MLT) [Ebihara and Ejiri, 2000]. Since no observation was carried out by NOAA 12 in the region between 2000 MLT and 0800 MLT, there is no way to find out where the peak of the ion flux occurs. In contrast to this, the peak of the proton flux inverted from the ENA emission

---

at 27–39 keV was clearly identified to be located near 0500 MLT during the main phase of the 4 October 2000 storm [*C:son Brandt et al.*, 2002b], which represented an extreme case of their data set. The postmidnight enhancement of the proton flux was also observed in the 119–198 keV energy range during the storm of 4 October 2000, meaning that this morphological feature commonly emerges in a wide energy range, at least between 27 and 198 keV for this particular storm. They suggested that the extreme postmidnight enhancement of this storm could also be due to an eastward skewing convection pattern caused by the large positive Y-component of the IMF, in addition to the closure of the ring current.

[4] Global distribution of the proton pressure or energy density has been constructed by compiling a large set of data from the AMPTE CCE [*De Michelis et al.*, 1999; *Lui*, 2003] and the Polar [*Ebihara et al.*, 2002] satellites. A peak of the proton energy density (1–200 keV) occurs near midnight during a storm main phase [*Ebihara et al.*, 2002], while the peak of the proton pressure (1–4000 keV) lies in the dusk-midnight sector during active periods of high *Kp* values [*Lui*, 2003]. However, such average distribution obtained from the in situ satellite data cannot resolve any instantaneous state of the ring current pressure or energy density distribution in response to instantaneous magnetospheric conditions. We are interested in understanding how the instantaneous magnetospheric conditions govern the peak of the proton flux in the inner magnetosphere. Rather than focusing on the plasma pressure or energy density, focusing on the flux in a narrowed energy range is preferable in order to understand the physics that governs the motion of particles because the plasma pressure or energy density includes contributions from particles in all the energy range with different drift velocities.

[5] There are primarily two possible mechanisms that result in the postmidnight enhancement: (1) deformation of the magnetospheric electric field (which acts as a driver of the magnetospheric protons) and (2) local-time dependence of the plasma sheet proton distribution (which acts as a source of the inner magnetospheric protons). As described in section 2, empirical electric field models predict the peak of the tens-of-keV ion flux located in the premidnight sector, which fail to explain the observed postmidnight enhancement. On the basis of data from the Assimilative Model of Ionospheric Electrodynamics (AMIE), *Boonsiriseth et al.* [2001] and *Chen et al.* [2003] have shown that convection electric fields are largely deformed during the intense magnetic storms, and hence the drift trajectory of the energetic particles becomes extremely complicated. Numerical simulations have shown that the inner magnetospheric convection electric field can be significantly modified by a presence of the region 2 field-aligned current generated by the ring current [e.g., *Wolf*, 1970, 1983; *Fok et al.*, 2001; *Ridley and Liemohn*, 2002; *Khazanov et al.*, 2003a; *Toffoletto et al.*, 2003]. Using the Comprehensive Ring Current Model (CRCM) [*Fok et al.*, 2001], *Fok et al.* [2003] have shown that the postmidnight flux enhancement appears when the convection electric field is self-consistently coupled with the plasma distribution in the inner magnetosphere. They concluded that the postmidnight enhancement is associated with the strong ion penetration

in the midnight-dawn sector and is a consequence of the magnetosphere-ionosphere coupling.

[6] There are a number of mechanisms that potentially produce the postmidnight enhancement of the proton flux and the ENA flux. The purpose of this study is to find the most probable mechanisms causing the postmidnight enhancement of the 39–50 keV protons and to investigate the factors influencing the global morphology of the storm-time energetic ion flux. In particular, we focused on the following six possible mechanisms: (1) shielding electric field, (2) gap between the region 2 field-aligned current and the auroral oval, (3) strong gradient in the conductivity near the terminator, (4) plasma sheet density, (5) plasma sheet temperature, and (6) local-time dependence of the plasma sheet density on the nightside. The first five mechanisms are related to the deformation of the convection electric field due to the additional ionospheric electric field driven by the region 2 field-aligned current. The last one is related to the local-time dependence of the source population that contributes to the ring current and does not involve the deformation of the convection electric field.

2. Traditional Description of the Storm-Time Flux Enhancement

[7] A commonly used model of the dawn-dusk convection electric field is the Volland-Stern type convection electric field model [*Volland*, 1973; *Stern*, 1975] that is expressed by

$$\Phi = AL^{\gamma} \sin \phi, \qquad (1)$$

where A is a factor providing strength of the convection electric field, L is the L value, γ is the shielding factor, and ϕ is the MLT. Unity γ provides a uniform pattern of the electric potential, and larger γ represents a shielding effect. A morphology of drift trajectories of charged particles under the dipole magnetic field, the Volland-Stern type convection electric field and the corotation electric field was studied by *Chen* [1970] for $\gamma = 1$ and *Ejiri* [1978] for $\gamma = 2$.

[8] For simplicity, consider a drift trajectory of an ion with equatorial pitch angle of 90° and the dipole magnetic field. If the first adiabatic invariant is conserved, the drift trajectory follows an equipotential line expressed by

$$q\Phi + \mu B = \text{const}, \qquad (2)$$

where q is charge, μ is the magnetic moment, and B is the magnetic field. Figure 1 shows an example of the drift trajectory of an ion with the magnetic moment of 32 eV/nT, corresponding to kinetic energy of 37 keV at $L = 3$ and 1.0 keV at $L = 10$. The Volland-Stern type model with $\gamma = 2$ was used to trace the equipotential lines, and the polar cap potential drop was set to 200 kV.

[9] The last-closed equipotential line, indicated with a dashed line, is the innermost boundary that is accessible from the nightside plasma sheet. This boundary reaches its minimum distance to the center of the Earth at dusk, and for
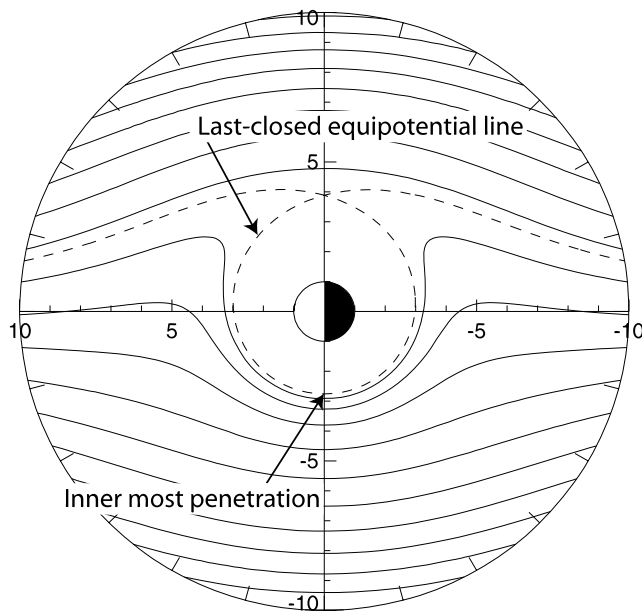
Figure 1. Example of drift trajectories of an ion with magnetic moment of 32 eV/nT (37 keV at $L = 3$) with equatorial pitch angle of 90° in the dipole magnetic field, the corotation electric field, and the Volland-Stern type convection electric field model with the shielding factor of 2. The dashed line indicates the last-closed equipotential line.

the given magnetic moment the kinetic energy is maximized at this point where the strength of the magnetic field is maximum. If the energy distribution of the phase space density of the ions decreases monotonically with energy, the differential flux would be the highest at this point, by applying the Liouville theorem.

[10] This interpretation is also valid for an ion with an arbitrary equatorial pitch angle when the first and second invariants are conserved. The differential ion flux is the highest at the minimum distance point where the strength of the magnetic field is the strongest and the length of the magnetic field line is the shortest.

[11] The simple Volland-Stern type model predicts the peak of the ring current ion flux ($> \sim 10$ keV) on the duskside but sometimes fails to explain the various MLT of the peak flux observed by the IMAGE/HENA, especially the postmidnight enhancements [C:son Brandt et al., 2002b]. Jordanova et al. [1999] simulated the ring current ions and compared it with the flux observed by the Polar satellite. They found that the simulated flux agrees with the observed one when the symmetry line of the Volland-Stern type convection electric field is artificially rotated by 3 hours eastward. Recently, Ebihara et al. [2004] have shown that a multiple-banded proton dispersion observed on the dayside is well explained by a simulation when the empirical convection model of Weimer [2001] is rotated by 2 hours eastward.

[12] The postmidnight enhancement may be accounted for by artificially rotating an empirical convection electric field model. However, our interest is in finding the most probable and essential physical mechanism causing the

postmidnight enhancement that may be related to the deformation of the convection pattern or some other possible processes.

3. Simulation

3.1. Kinetic Equation

[13] The CRCM [Fok et al., 2001] self-consistently solves the kinetic equation of ring current protons and the closure of the electric current between the magnetosphere and ionosphere. The particle is specified by a four-dimensional phase space density f as a function of magnetic latitude l_i, MLT ϕ_i, the first invariant M, and the second invariant K. The coordinate system is defined at the ionosphere altitude of 100 km. The first and second invariants are given by

$$M = \frac{p^2 \sin^2 \alpha}{2m_0 B}, \qquad (3)$$

$$K = \int_{sm_1}^{sm_2} \sqrt{B_m - B(s)} \, ds, \qquad (4)$$

where p is the momentum, α is the pitch angle, m_0 is the rest mass, and B_m is the magnetic field at the mirror points sm_1 and sm_2. The phase space density specified by M and K can be easily mapped to the phase space density specified by the kinetic energy and the equatorial pitch angle.

[14] The evolution of particle phase space density can be described by the bounce-averaged Boltzmann equation,

$$\frac{\partial \overline{f}_s}{\partial t} + \langle \dot{l}_i \rangle \frac{\partial \overline{f}_s}{\partial l_i} + \langle \dot{\phi}_i \rangle \frac{\partial \overline{f}_s}{\partial \phi_i} = -v\sigma_s \langle n \rangle \overline{f}_s - \left(\frac{\overline{f}_s}{0.5\tau_b} \right)_{\text{loss cone}}, \quad (5)$$

where $\overline{f}_s = \overline{f}_s(l_i, \phi_i, M, K)$ is the four-dimensional phase space density, v is the velocity of particle, σ_H is the cross section for charge exchange, n is the density of neutral atoms, and τ_b is the bounce period. The operator $\langle \rangle$ stands for a quantity bounce-averaged over a field line between two mirror points sm_1 and sm_2. The atmospheric absorption altitude for the ions is defined at 100 km altitude. The bounce-averaged drift velocities, $\langle \dot{l}_i \rangle$ and $\langle \dot{\phi}_i \rangle$, are described by Fok and Moore [1997].

3.2. Magnetic Field Model

[15] We used the empirical magnetic field model of Tsyganenko [1995] and Tsyganenko and Stern [1996]. This model provides the external magnetic field parameterized by the solar wind dynamic pressure, the Dst index, IMF By, and Bz. The parameters were chosen from observed data at the beginning of the simulation, and were held constant throughout the simulation to avoid the effects of time-varying magnetic field in order to highlight a particular effect that we focused on.

3.3. Electric Field Model

3.3.1. Self-Consistent Electric Field

[16] An incomplete closure of the gradient and curvature drift currents in the magnetosphere produces field-aligned
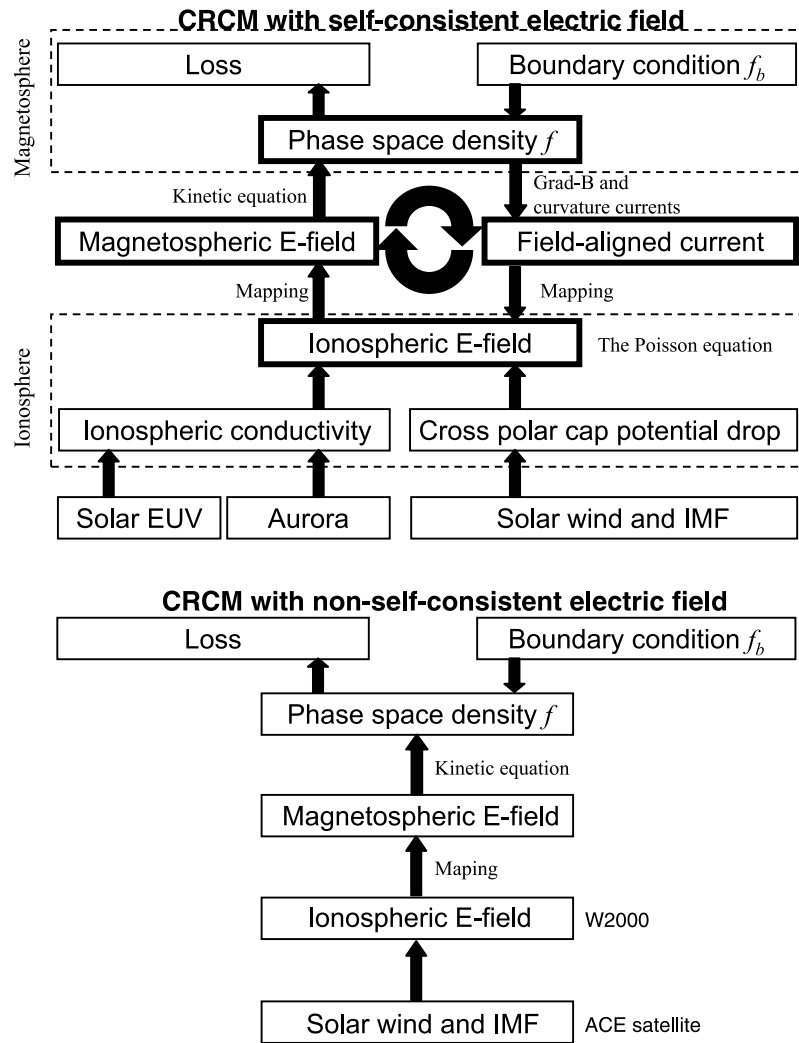
Figure 2. Block diagrams of the CRCM with the self-consistent electric field (top) and with the non-self-consistent electric field (bottom).

currents connecting with the ionosphere. This condition occurs when the pressure gradient vector is not perpendicular to the grad-B and curvature drift velocity. Assuming the current continuity ($\nabla \cdot \mathbf{J} = \mathbf{0}$), the ionospheric electric potential can be calculated from the requirement that the ionosphere conducts away the charge deposited by the field-aligned currents. The calculation of the ionospheric electric potential was performed by using the algorithm of the Rice Convection Model (*Harel et al.* [1981] and *Toffoletto et al.* [2003] for review). The outer boundary to solve the ionospheric electric field was fixed at 66.7 deg magnetic latitude at 100 km altitude for this particular study. This would slightly underestimate (overestimate) the ionospheric electric field when the actual polar cap latitude is lower (higher) than 66.7 deg.

[17] The polar cap potential (PCP) drop was imposed at the poleward boundary of the simulation region in the ionosphere. Two empirical models of the PCP Φ_P were used. The first one is the *Weimer* [2001] model (hereinafter

referred to W2000) based upon satellite measurements made by the Dynamics Explorer-2 satellite on 2645 polar cap passes. The electric potential is expressed by a spherical harmonic series as

$$\Phi(\phi, \theta) = \sum_{l=0}^{4} \sum_{m=0}^{\min(l,3)} (A_{lm} \cos m\phi + B_{lm} \sin m\phi) P_l^m(\cos\theta), \quad (6)$$

where θ is the geomagnetic colatitude and P_l^m is the associated Legendre function. The spherical harmonic coefficients A_{lm} and B_{lm} depend on the solar wind velocity, IMF, and the dipole tilt angle of the Earth's rotation. The electric potential distribution at the poleward boundary of the CRCM was imposed in solving the Poisson equation.

[18] Another model of the PCP is from the *Boyle et al.* [1997] model (hereinafter referred to the B1997 model), based upon plasma flow measurements by DMSP F8 and F9

Table 1. Summary of the Events Studied in This Study

Date,	Time, UT	Dst nT	Kp	Daily $F10.7$	IMAGE SM X, R_E	SM Y, R_E	SM Z, R_E
12 August 2000	0940	−235	8^-	194.3	−0.54	0.15	6.74
29 October 2000	0320	−127	6	184.5	−0.11	0.19	7.59
3 October 2001	1140	−142	7	191.8	0.08	1.51	7.67
21 October 2001	1900	−115	7^+	222.0	−2.29	−0.25	5.54
20 April 2002	0540	−145	7^+	181.4	0.09	0.47	6.34

satellites. The PCP is given by a mathematical expression with its coefficients depending on the solar wind velocity and IMF.

$$\Phi_P = 1.1 \times 10^{-4} V_{sw}^2 + 11.1 B_{IMF} \sin^3\left(\frac{\theta_{IMF}}{2}\right) \quad \text{(kV)}, \quad (7)$$

where V_{sw} is the solar wind velocity in km/s, B_{IMF} is the magnitude of IMF in nT, and θ_{IMF} is the clock angle of IMF.

[19] The International Reference Ionosphere (IRI-95) [*Bilitza*, 1997] model and the Mass Spectrometer Incoherent Scatter (MSIS-E90) model [*Hedin*, 1991] were employed to calculate the background Pedersen and Hall conductivities. As for the aurora-associated conductivity, we used the empirical model of *Hardy et al.* [1987], who calculated the Hall and Pedersen conductivities for different Kp levels, based on the empirical model of energy flux and average energy of precipitating electrons [*Hardy et al.*, 1985].

[20] The electric potential in the ionosphere was mapped along a field line under the assumption that the field line is equipotential. The newly updated electric field was used to solve the kinetic equation (5). The logic of the CRCM that takes into account the self-consistent electric field is schematically drawn in the top panel of Figure 2. We used the solar wind and IMF data from the ACE satellite, and the time lag between the ACE satellite and the Earth was taken into consideration.

3.3.2. Non-Self-Consistent Electric Field

[21] The non-self-consistent electric field model, the W2000 model, was used to exclude the effect of the deformation of the convection electric field caused by the presence of the region 2 field-aligned current. The electric field is independent of the condition of the simulated ring current. The logic of the simulation with the non-self-consistent electric field is schematically drawn in the bottom panel of Figure 2.

3.4. Boundary and Initial Conditions

[22] The outer boundary for the particle injection was located at the radial distance of 10 R_E in the equatorial plane. We consider only protons, and the distribution function at the outer boundary was held constant and assumed to be isotropic Maxwellian with density of 0.5 cm^{-3} and temperature of 5 keV unless otherwise mentioned. The magnetosphere was initially filled with preexisting particles with the distribution function measured by AMPTE/CCE in quiet time [*Sheldon and Hamilton*, 1993].

3.5. ENA Calculation

[23] The directional differential flux of the energetic neutral hydrogen is given by a line-of-sight integral,

$$j_{ENA}(E) = \sum_s \int j_{proton}(\mathbf{r}, \mathbf{E}, \mathbf{a}) \mathbf{n_s}(\mathbf{r}) \sigma_{ps}(\mathbf{E}) \mathbf{dl}, \quad (8)$$

where $j_{proton}(\mathbf{r}, E, \alpha)$ is directional differential flux of proton, $\mathbf{r}$ is vector of position, $n_s(\mathbf{r})$ is number density of neutral of species s, and $\sigma_{p,s}(E)$ is charge exchange cross section between proton and neutral of species s. Knowing the equatorial pitch angle (α_0), the local pitch angle (α) is obtained by assuming the conservation of the first invariant, that is, $\sin\alpha = \sin\alpha_0\sqrt{B/B_0}$, where B is the local magnetic field, and B_0 is the equatorial magnetic field.

[24] We assume that the two charge exchange reactions, $H^+* + H \rightarrow H^* + H^+$ and $H^+* + O \rightarrow H^* + O^+$, dominate in the generation process of the energetic neutral hydrogen observed by IMAGE/HENA, where the superscript * stands for energetic. The stripping collision, the ionization collision, the excitation collision, and all the secondary products among these reactions were not taken into account in the calculation. If we focus on the MLT-dependence of the ENA emission, the global morphology of the emission would not be strongly affected by these collisional processes when viewed from above the magnetic pole.

[25] We used the charge exchange cross sections given by *Barnett* [1990] for $\sigma_{p,H}$, *Stancil et al.* [1999] for $\sigma_{p,O}$, the neutral density models given by *Rairden et al.* [1986] for neutral hydrogen density n_H, and MSIS-E90 [*Hedin*, 1991] for neutral oxygen density n_O. Two-dimensional ENA images were simulated by performing the line-of-sight integral (8) from the IMAGE position and were projected in a fish-eye view to compare with the IMAGE/HENA observations.

4. Result

4.1. Deformation of the Convection Electric Field

[26] *C:son Brandt et al.* [2002b] found 18 observations of the storm-time ENA during the periods that satisfy the following three criteria: (1) The observation was made during the magnetic storm that reaches minimum Dst of −50 nT or less. (2) The period of southward IMF remained for 3 hours and more. (3) The IMAGE satellite was nearly over the magnetic north pole. Five of them were selected for this study with an additional criteria that the Dst index was −100 nT or less at the moment of the observation. Table 1 summarizes the Dst index, the Kp index, the daily $F10.7$ index, and the IMAGE position in the SM coordinates for the five observations.

[27] Figure 3 shows the ENA flux from IMAGE/HENA (left), the ENA flux from CRCM (middle), and the simulated proton flux averaged over pitch angle in the equatorial plane (right) for the five storms: 12 August 2000, 29 October 2000, 3 October 2001, 21 October 2001, and 20 April 2002. The PCP drop was calculated by using the W2000 model that depends on the solar wind and IMF, and the convection electric field was self-consistently calculated. The peak of the simulated ENA flux, indicated by a red area, is shown to occur in the midnight-
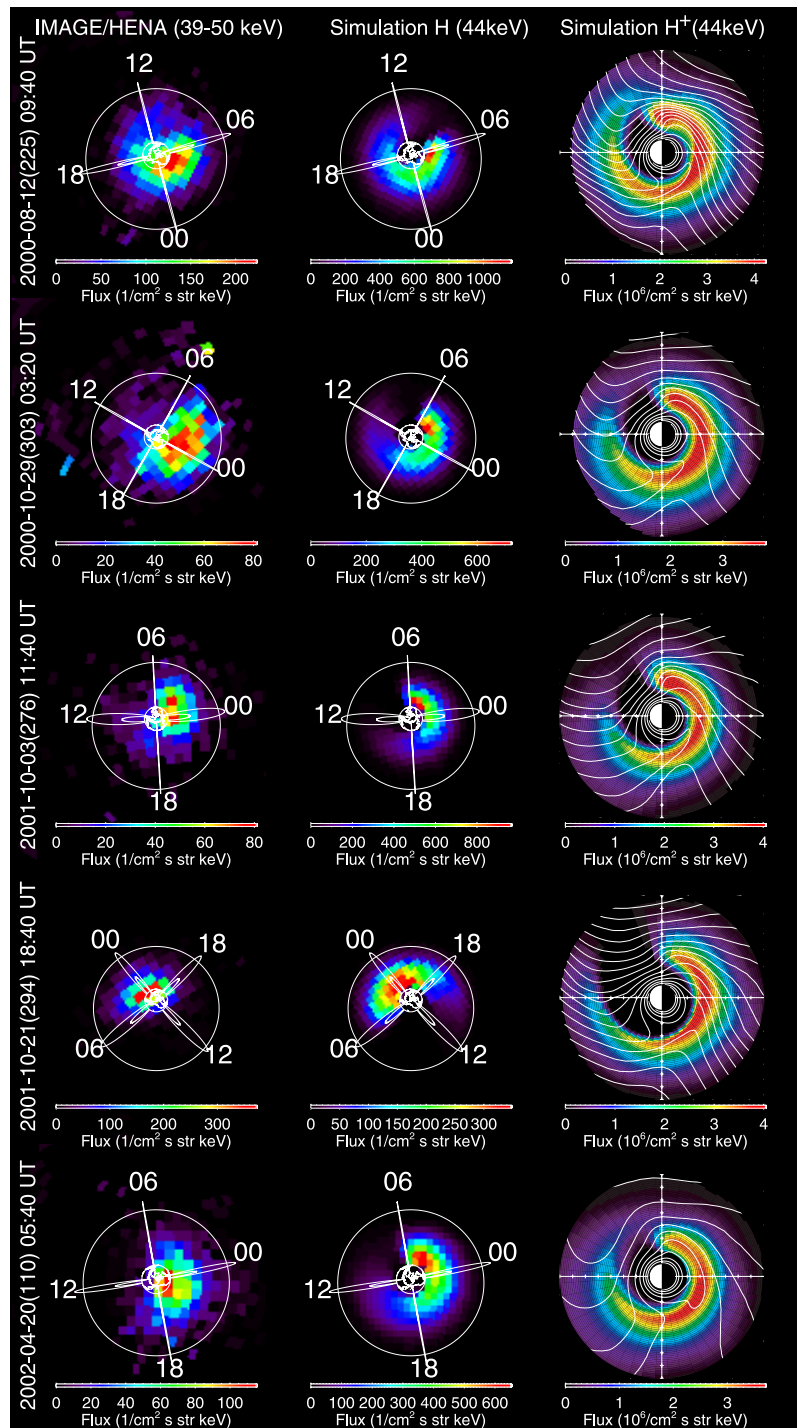
Figure 3. (left) Observed ENA flux at 39–50 keV, (middle) simulated ENA flux at 44 keV, and (right) simulated proton flux averaged over pitch angle in the equatorial plane for the five storms. The PCP was given by the empirical model of W2000. Dipole magnetic field lines for $L = 3$ and 6.6 are indicated with white lines at 0000, 0600, 1200, and 1800 MLT in the left and middle panels. In the right panel, white contour lines mark the calculated convection electric potentials including corotation electric field.

dawn sector and to depend on storms. In general, a morphological feature of the simulated ENA fluxes agrees well with the observation in terms of the MLT value at which the emissions peak.

[28] The convection electric potential (indicated with a white lines on the right panel) is shown to be greatly distorted from a simple dawn-dusk electric electric field, especially in the midnight-dawn sector. The distortion skews the drift trajectory significantly, and as a consequence, the peak MLT moves eastward. This distortion of the convection field is discussed by *Wolf* [1983] in detail and can be primarily caused by the following three mech-
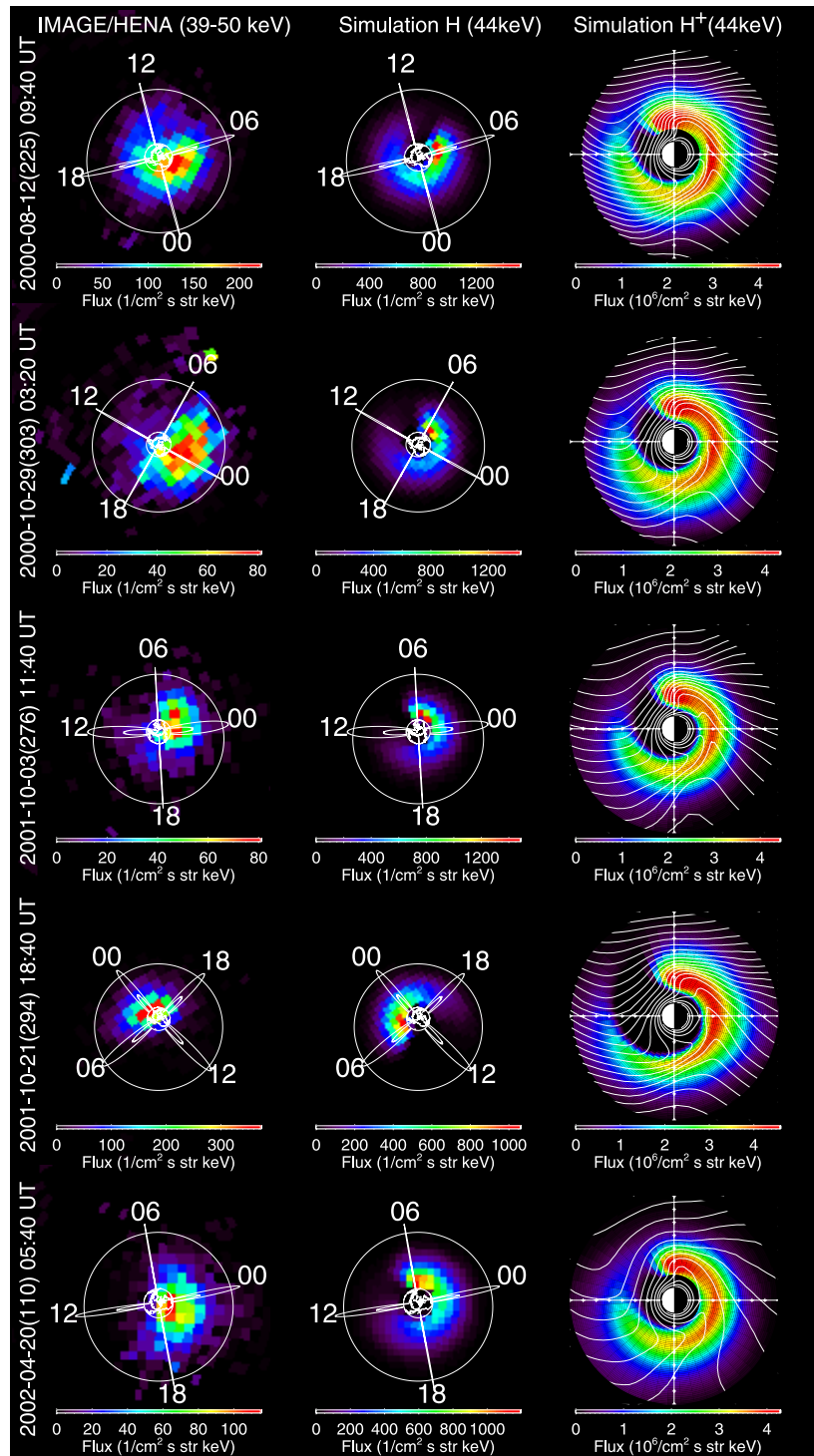
Figure 4. Same as Figure 3 except that the PCP was given by the empirical model of B1997.

anisms: (1) shielding electric field driven by the region 2 field-aligned current, (2) gap between the auroral oval and the region 2 field-aligned current, and (3) conductivity gradient near the terminator. These mechanisms are discussed in detail later. The empirical convection model W2000 does not show this strong distortion. *Fok et al.* [2003] have emphasized that the convection model W2000 preferably results in the peak MLT in the premidnight sector, which is inconsistent with the IMAGE/HENA observation.

[29]   An interesting feature is found in the bottom panel of Figure 3, where the ENA emission and proton flux for the storm of 20 April 2002 are displayed. The simulated proton flux peaks in the premidnight sector, while the simulated ENA flux peaks in the postmidnight sector. That is because the field-aligned flux dominates over the perpendicular flux
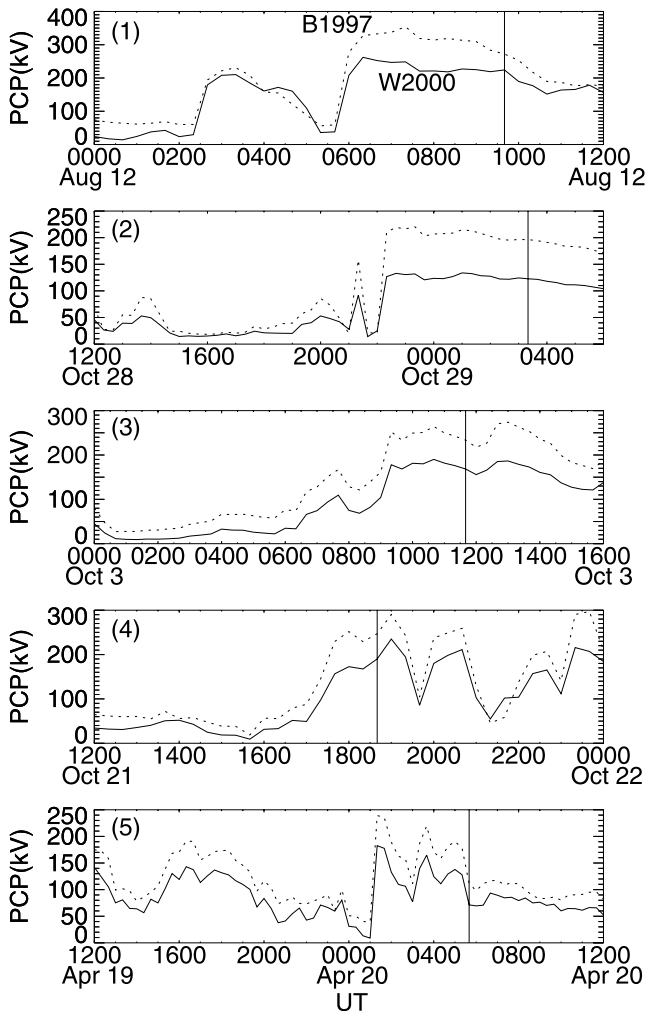
Figure 5. PCPs calculated by the W2000 model (solid line) and the B1997 model (dotted line) for the five storms of (1) 12 August 2000, (2) 29 October 2000, (3) 3 October 2001, (4) 21 October 2001, and (5) 20 April 2002.

in the postmidnight sector during this particular period. The time-dependent behavior of the convection electric field makes it difficult to comprehend why the field-aligned flux dominates in the postmidnight sector. One simple explanation is that the grad-B and curvature drift depending on the energy results in the flux distribution dominated by the field-aligned component in the postmidnight region. In case of the dipole magnetic field, the magnetic drift velocity of a charged particle with an equatorial pitch angle of 90° is about 1.5 times larger than with an equatorial pitch angle of 0° [*Ejiri*, 1978]. Since the direction of the magnetic drift is westward for ions, the ions with field-aligned equatorial pitch angle tend to remain in the postmidnight region. According to an in situ measurement performed by Explorer 45, a newly injected ion flux with 30° pitch angle was observed to be greater than with 90° pitch angle in the 0130–0215 MLT range [*Ejiri et al.*, 1980]. The ENA emission is shown to be sensitive to the pitch angle distribution of the proton flux because strong emissions of ENAs come from the region where the neutral density is high and/or the proton flux is high.

[30] Figure 4 also shows a comparison between the observed ENA emission and the simulated one in case of using the B1997 model for PCP, instead of using the W2000 model. There is a clear tendency that the simulated peak MLT is located farther eastward than the observed one. This suggests that the overall convection strength in terms of the PCP has a significant influence on the morphology of the distributions of the proton flux and the ENA flux.

[31] When the PCP is high, the plasma sheet protons drift deeper into the inner region, and the protons generate the stronger region 2 field-aligned current that in turn, leads to the highly deformed convection pattern in the postmidnight region. As a result, the peak of the proton flux moves eastward when the PCP is high.

[32] Figure 5 shows a comparison between the PCPs obtained by the W2000 model and the B1997 model during the five storms that we simulated. The comparison indicates that the PCP modeled by B1997 tends to be higher than modeled by W2000. This tendency has been pointed out by *Ober et al.* [2003], who compared with the DMSP observation and the *Hill et al.* [1976] model. They reported that for strongly southward IMF conditions the B1997 model tends to predict larger PCPs than observed PCPs, while the PCPs predicted by the W2000 model and the *Hill et al.* [1976] model generally fit the observations much better.

[33] Comparison between Figures 3 and 4 also serves to conclude that the B1997 model probably overestimates the PCP because the B1997 model results in too much deformation of the convection electric field, and the peak MLT of the ENA emission is located farther eastward than the observed one. The W2000 model seems to provide a more realistic PCP in terms of the peak MLT or the deformation of the convection.

4.1.1. Effect of Conductivity Gradient Near the Terminator

[34] *Wolf* [1970] has pointed out that a strong gradient of the ionospheric conductivity near the terminator deforms the convection pattern significantly. On the dawnside, the Hall current flows generally westward along an equipotential line in the ionosphere. The conductivity is much smaller on the nightside than on the dayside, and the strong gradient of the Hall conductivity near the terminator causes an excess of positive charge near the terminator. To satisfy the current continuity ($\nabla \cdot \mathbf{J} = \mathbf{0}$), the Pedersen currents, which are generally equatorward, have to increase. This requires additional equatorward electric fields, and hence deforms the convection pattern significantly near the terminator.

[35] In order to exclude the effect of the strong conductivity gradient, we performed a simulation with the assumption that the background Pedersen and Hall conductivities are uniform and equal to 10 mho. The aurora-associated conductivity was included. The W2000 model was used to provide the polar cap potential, and the convection electric field was self-consistently calculated. The result is displayed in the top panel of Figure 6 showing that there is a postmidnight enhancement of the ENA emission, even though the background conductivity is uniform. It should be noted that the peak of the ENA emission seems to be broadened when there is no conductivity gradient between the dayside and nightside. The conductivity gradient near the terminator is found to favor strong ENA emission at
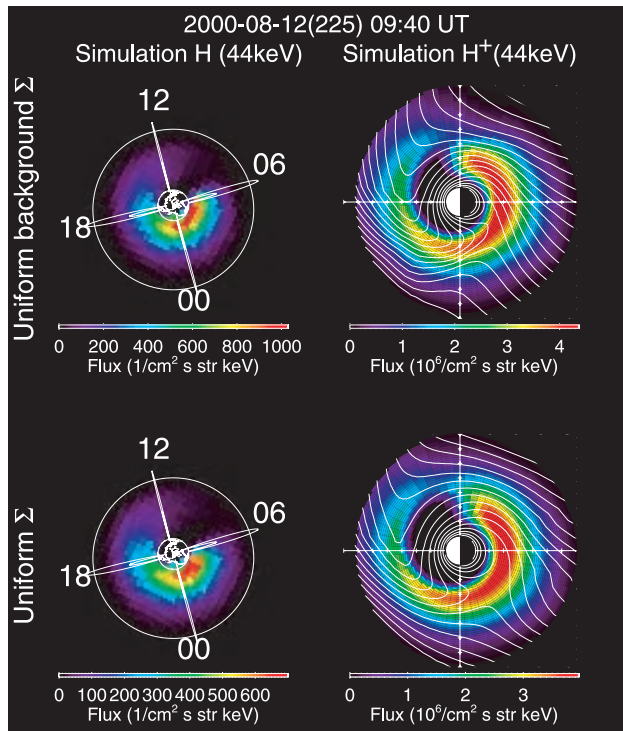
Figure 6. Same as the top panel of Figure 3 except that (top) only the background Pedersen and Hall conductivities were uniform to 10 mho and (bottom) the conductivities were completely uniform to 10 mho.

dawn but appears not to be a necessary condition in causing the postmidnight enhancement.

4.1.2. Effect of the Auroral Oval

[36] The equatorward edge of the main auroral oval may correspond to the inner edge of the electron plasma sheet. As the plasma sheet electrons drift sunward by the convection electric field in the magnetosphere, they tend to drift eastward due to the grad-B and curvature drifts. Meanwhile, the plasma sheet ions tend to drift westward. As a result, the ions drift earthward deeper than the electrons on the duskside. In most cases the plasma pressure that generates the region 2 field-aligned current is dominated by the ions, whereas the main auroral oval is brought by precipitation of the plasma sheet electrons. This separation causes a gap between the region 2 field-aligned current and the auroral oval on the duskside [*Toffoletto et al.*, 2003, and references therein].

[37] In order to exclude the effect of the gap between the region 2 field-aligned current and the auroral oval, we performed a simulation with the assumption that the conductivity is completely uniform. The bottom panel of Figure 6 shows the ENA emission in case of a completely uniform conductivity. The Pedersen and Hall conductivities were set to 10 mho. The result shows that the intensity of the electric field at dusk is weakened because of absence of the large conductivity associated with the auroral precipitation. However, there seems no appreciable difference between the two cases in terms of the ENA emission; one includes the aurora-associated conductivity (top), and another one excludes the aurora-associated conductivity (bottom).

[38] This means that the gap between the region-2 field-aligned current and the auroral oval is not important for the generation of the postmidnight enhancement. If the postmidnight enhancement is primarily caused by the deformation of the convection electric field, it would be reasonable to conclude that the shielding is probably the prime mechanism, followed by the conductivity gradient near the terminator, and the gap between the region 2 field-aligned current and the auroral oval is probably a minor mechanism.

4.1.3. Effect of the Solar Radiation

[39] The ionospheric conductivity is expected to influence greatly the degree of the shielding because the intensity of the shielding electric field is approximately proportional to the reciprocal of the Pedersen conductivity. The $F10.7$ index of 194.3 (corresponding to that of 12 August 2000) was used to calculate the emission shown in Figure 3. Figure 7 shows the ENA emission in cases of low conductivity due to low solar radiation ($F10.7 = 70$) and high conductivity due to high solar radiation ($F10.7 = 250$). The condition of the ionospheric conductivity was changed by putting the $F10.7$ value into the MSISE-90 and IRI-95 models. The peak MLT is located at ~0600 MLT for $F10.7 = 70$ (the solar minimum condition), while at ~0500 MLT for $F10.7 = 250$ (the solar maximum condition). It can be seen that the low ionospheric conductivity results in the peak MLT located slightly eastward.

4.1.4. Effect of Plasma Sheet Density

[40] The plasma sheet density influences the morphology of the convection pattern [e.g., *Jaggi and Wolf*, 1973;
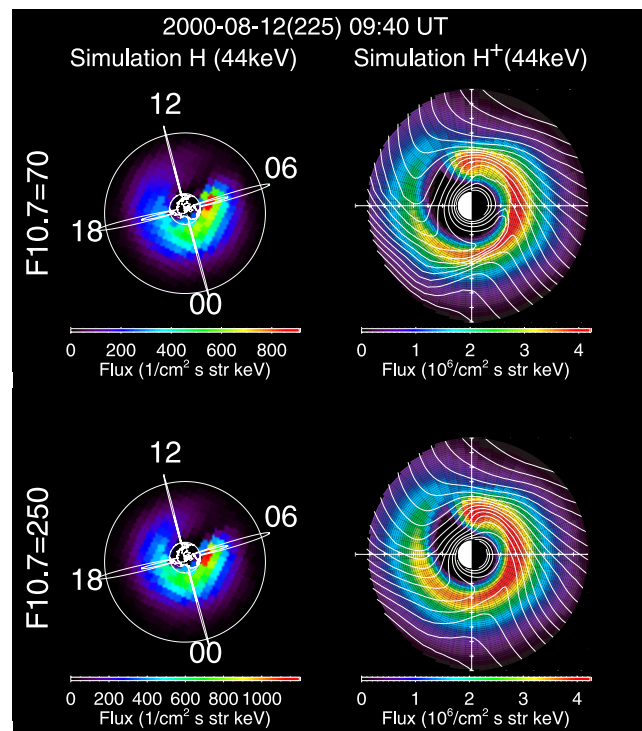

Figure 7. Same as the top panel of Figure 3 except for the background conductivity for (top) $F10.7 = 70$ and (bottom) $F10.7 = 250$.
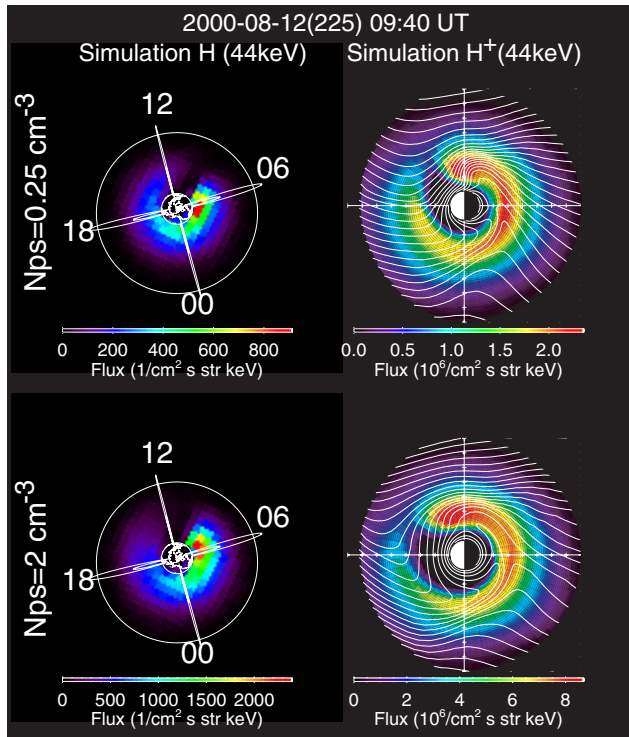
Figure 8. Same as the top panel of Figure 3 except that the plasma sheet density was held constant to (top) 0.25 cm^{-3} and (bottom) 2 cm^{-3}. The plasma sheet temperature was set to 5 keV.

Garner, 2003]. *Jaggi and Wolf* [1973] have shown that the inner most penetration distance of the plasma sheet ions depends on the plasma sheet density. *Garner* [2003] has demonstrated that the degree of the deformation of the convection electric field becomes large when the plasma sheet density is high.

[41] The plasma sheet density of 0.5 cm^{-3} was used to calculate the emission shown in Figure 3. Figure 8 shows the simulated ENA emissions in cases of low plasma sheet density, 0.25 cm^{-3}, and high plasma sheet density, 2.0 cm^{-3}. An isotropic Maxwellian distribution was assumed, and the plasma sheet temperature was kept constant to 5 keV. The W2000 model was used to calculate the PCP, and the convection electric field was self-consistently calculated.

[42] When the plasma sheet density increases from 0.25 cm^{-3} to 2.0 cm^{-3}, the peak MLT moves eastward from ∼0500 MLT to ∼0700 MLT. This azimuthal shift of the peak is reasonably attributed to the development of the deformation of the convection electric field driven by the increased region 2 field-aligned current. Dense plasma sheet particles simply increase the intensity of the region 2 field-aligned current.

4.1.5. Effect of Plasma Sheet Temperature

[43] Figure 9 shows the simulated ENA emissions in case of a plasma sheet temperate ranging between 2 keV and 11 keV. The plasma sheet density was kept constant to 0.5 cm^{-3}, and the W2000 model was used to calculate the PCP. The peak MLT is obviously found to persist at dawn, regardless of the variation of the plasma sheet temperature,

meaning that the plasma sheet temperature is not effective in controlling the peak MLT and the morphology of the ENA emission. When the plasma sheet temperature is high, the spatial distribution of the ion flux in the equatorial plane tends to be extended in *L*, reflecting the change that the high-energy tail in the ion distribution in the plasma sheet is raised with increasing temperature. This means that hot plasma sheet particles do not simply increase the intensity of the region 2 field-aligned current. Hence there is no morphological change in the equatorial proton flux significantly in terms of MLT.

4.2. Localized Enhancement of the Plasma Sheet Density

[44] We assumed that the plasma sheet density is independent of MLT in the previous section. In order to investigate another prime mechanism, local-time depen-
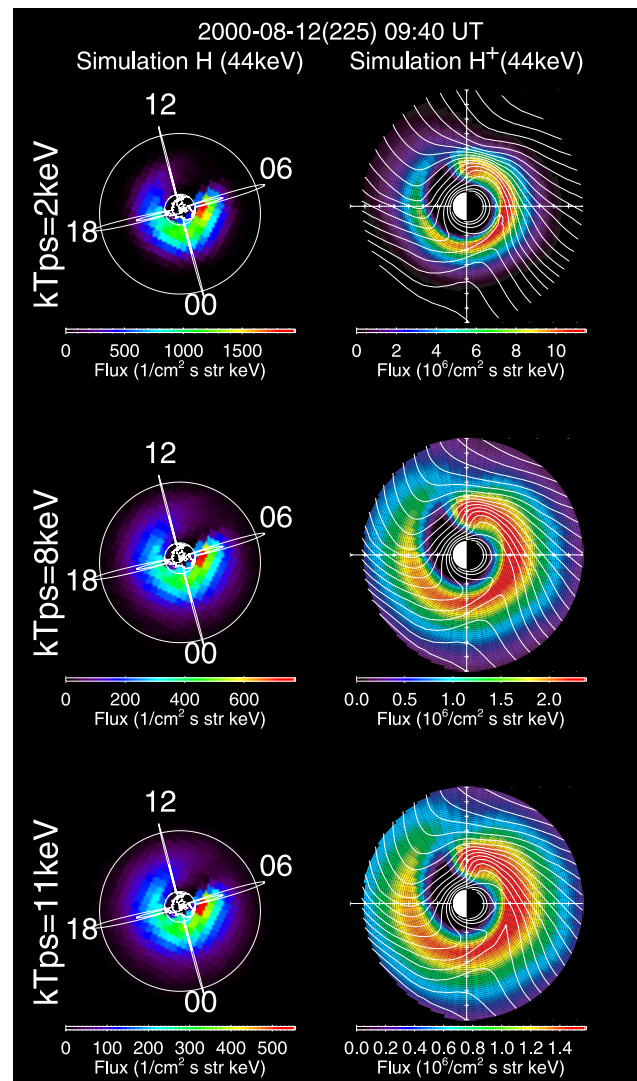

Figure 9. Same as the top panel of Figure 3 except that the plasma sheet temperature was held constant to (top) 2 keV, (middle) 8 keV, and (bottom) 11 keV. The plasma sheet density was set to 0.5 cm^{-3}.
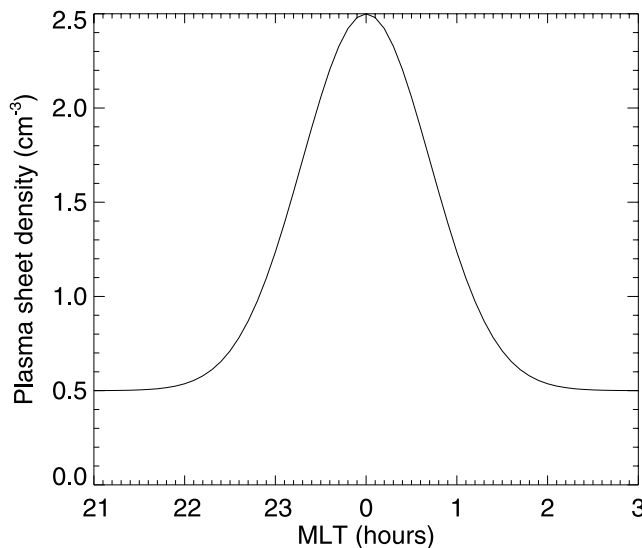
Figure 10. Modeled plasma sheet density as a function of MLT.

dence of the plasma sheet ion distribution, we modeled a simple distribution of the plasma sheet density that has a single peak at midnight,

$$N_{ps}(\phi) = 0.5 \left[1 + 4 \exp \left(-\frac{(\phi - \phi_0)^2}{\Delta\phi^2} \right) \right] \text{cm}^{-3}, \qquad (9)$$

where $\Delta\phi$ is a half of the characteristic width of the localized enhancement, and ϕ_0 is the MLT at the peak. Here ϕ_0 and $\Delta\phi$ were set to be 0000 MLT and 1 hour, respectively. The modeled MLT variation of $N_{ps}(\phi)$ is shown in Figure 10. The density at midnight is 5 times higher than ambient. To exclude the effect of the deformation of the convection electric field caused by the region 2 field-aligned current, we used entirely the W2000 convection electric field model, that is, the convection electric field is now independent of the condition of the simulated ring current.

[45] Figure 11 shows the simulated ENA and proton fluxes in case of the plasma sheet density depending on MLT. The postmidnight enhancement appears clearly, and the morphological feature of the simulated ENA emission agrees well with the observation on the nightside. However, a disagreement is found on the dayside. The simulated ENA emission shows a "tail-like" structure extending from the nightside to the dayside. The corresponding proton flux displays two peaks both on the nightside and dayside.

[46] To understand the formation of the double peaks, suppose the plasma sheet protons departs the plasma sheet near midnight because the plasma sheet density at midnight is higher than in other MLTs for this particular simulation. If the first two adiabatic invariants are conserved, the plasma sheet proton would gain kinetic energy on the nightside and would lose the kinetic energy on the dayside as the proton moves along its drift trajectory (c.f., Figure 1). There are two points at which the proton has the same energy along its drift trajectory. One point is on the nightside, and another one is on the dayside. When a detector observes particles at a given energy, the detector observes the double-peaked structure of the protons on the nightside and the dayside. The dayside peak is an approximate reflection of the nightside one about the dawn-dusk meridian.

[47] *C:son Brandt et al.* [2002a] calculated the global distribution of tens-of-keV proton flux for the case that the plasma sheet injection is azimuthally localized and showed the double-peaked structure. They attributed the tens-of-keV ENA emission peaking at ∼0300 MLT, observed by the Astrid 1 satellite, to a narrow injection channel in the nightside plasma sheet.

[48] The possibility of this mechanism, a localized enhancement of the plasma sheet density, can be justified by measuring carefully the ENA emission coming from the dayside magnetosphere. If the intensity of the dayside ENA emission is comparable to the nightside one, this possibility will be plausible. However, the data from IMAGE/HENA (Figure 3) shows that the dayside emission seems faint as compared with the nightside emission for these particular observations. This indicates that the localized enhancement of the plasma sheet density is unlikely unless the dayside emission is manifest. Careful investigation and diagnosis have to be performed in the future to reach a definitive conclusion whether the localized enhancement of the plasma sheet density is the most prob-
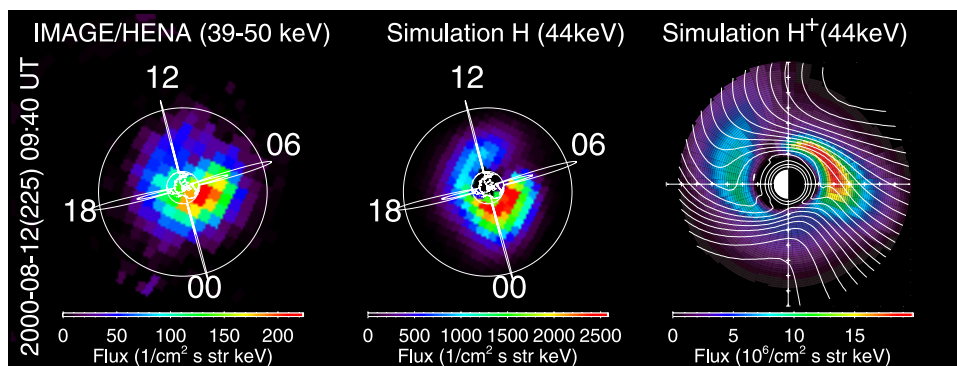

Figure 11. Same as the top panel of Figure 3 except that the plasma sheet density at midnight is 5 times higher than ambient.

able mechanism in producing the postmidnight enhancement of the proton flux.

5. Discussion

[49] We have shown that the postmidnight flux enhancement can be caused by at least the two prime mechanisms: (1) deformation of the convection electric field due to the shielding electric field and/or (2) local-time dependence of the plasma sheet density. However, there are probably more mechanisms that can explain the postmidnight enhancement and/or controlling the peak MLT. First, depression and inflation of the equatorial magnetic field due to the enhanced ring current is found to modify significantly the drift trajectory of the ring current particles [c.f., *Ebihara and Ejiri*, 2000, Figure 10]. A self-consistent magnetic field model that couples with the pressure distribution of the ring current must be developed to test this mechanism.

[50] Second, a highly skewed convection pattern due to IMF *By* [*Khurana et al.*, 1996] may control the peak MLT significantly, as suggested by *C:son Brandt et al.* [2002b]. In principle, a midnight-noon polarization electric field induced by the nonuniformity of the ionospheric conductivity rotates clockwise the entire convection patterns of the northern hemisphere and southern hemisphere when viewed from above the north magnetic pole [*Crooker and Siscoe*, 1981]. In the northern polar cap, the rotation of the convection pattern caused by IMF *By* is predicted to be in the opposite sense to that in the southern polar cap [*Khurana et al.*, 1996]. The rotation due to IMF *By* is known to be significant for the polar cap region (or the lobe region), but the overall contribution on rotating the convection pattern in the inner magnetosphere ($L \sim 3$) where the magnetic field line is tightly closed is debatable.

[51] Third, local-time dependence of the proton loss is a good candidate of the asymmetric distribution of the flux. *Anderson et al.* [1992] have shown that the wave activity in the Pc 1−2 range, identified as electromagnetic ion cyclotron (EMIC) waves, is highly local-time dependent at $L > 7$. Numerical simulations have shown that the distribution of the wave activity is spatially localized and located primarily on the duskside [*Jordanova et al.*, 1997; *Khazanov et al.*, 2003b]. The wave activity will scatter trapped protons in the magnetosphere and will result in an overall reduction of the proton flux, and hence the corresponding ENA emission will be weakened. Some scattered protons will fall into the ionosphere and will emit an ENA at low altitudes where the neutral density is high, and hence the corresponding ENA emission will be strengthened. The overall contribution of the wave activity to the development of the postmidnight enhancement is also unsettled.

6. Conclusion

[52] Using the self-consistent simulation called CRCM, we investigated physical mechanisms that govern the global morphology of the 39−50 keV flux. The primary results can be summarized as follows.

[53] 1. It is a natural behavior in the simulation that when the PCP strength is high, the peak MLT of tens-of-keV ENA emissions appears in the postmidnight sector, even though the plasma sheet density is azimuthally uniform.

[54] 2. The shielding electric field seems to be the most significant factor in producing the postmidnight enhancement, followed by the conductivity gradient near the terminator. The conductivity gradient near the terminator sharpens the region of the ENA emission. Contribution from changes in the electric field due to the gap between the region 2 field-aligned current and the auroral oval is negligible.

[55] 3. The ENA emission simulated with the PCP modeled by B1997 disagrees with the IMAGE/HENA observation in terms of MLT value at which the emissions peak. The agreement is improved when the PCP is modeled by W2000. The PCP strength is thus important in controlling the peak MLT value.

[56] 4. The peak of the ENA emission shifts eastward when the background conductivity is low (or in the solar minimum condition). Significant earthward penetration of the plasma sheet ions occurs where the $\mathbf{E} \times \mathbf{B}$ drift velocity is earthward. When the ions drift earthward, the ion gains kinetic energy adiabatically and the ion flux increases. The peak of the ENA emission roughly occurs where the ion gains the highest kinetic energy and lies near dawn when the ionosphere is coupled with the ring current. When the ionosphere conductivity is low, the eastward-directed shielding electric field is enhanced on the nightside, resulting in eastward rotation of the region where the $\mathbf{E} \times \mathbf{B}$ drift velocity is earthward.

[57] 5. The peak shifts eastward when the plasma sheet density is high. The high plasma sheet density enhances the region 2 field-aligned current, strengthening the eastward-directed shielding electric field.

[58] 6. The peak MLT value is less dependent of the plasma sheet temperature because the hot plasma sheet does not simply enhance the region 2 field-aligned current.

[59] 7. The localized enhancement of the plasma sheet density results in the postmidnight enhancement without introducing the self-consistent electric field. Strong emissions are, however, expected to appear on both the nightside and the dayside. The possibility can be justified by a careful observation in the dayside magnetosphere.

[60] All the possible mechanisms contribute to the global morphology of the proton flux distribution. However, it is impossible to definitively determine which mechanism dominates unless performing direct measurements of the electric field and the proton fluxes simultaneously. Data from radar or ground magnetometers are necessary to infer the global distribution of the convection electric field. Data from a constellation of the geosynchronous orbit satellites (i.e., the LANL satellites) are useful to measure the local-time dependence of the plasma sheet proton distribution. A comprehensive study using observational and simulational data should be conducted in the future to conclude more definitively which mechanism dominates the global distribution of the proton fluxes.

References

Anderson, B. J., R. E. Erlandson, and L. J. Zanneti (1992), A statistical study of Pc 1−2 magnetic pulsations in the equatorial magnetosphere: 1. Equatorial occurrence distributions, *J. Geophys. Res.*, 97, 3075.

Barnett, C. F. (1990), Atomic data for fusion, volume I: Collisions of H, H2, He, and Li atoms and ions with atoms and molecules, *Tech. Rep. ORNL-6086/V1*, Oak Ridge Nat. Lab., Oak Ridge, Tenn.

Bilitza, D. (1997), International Reference Ionosphere-status, 1995/96, *Adv. Space Res.*, 20, 1751.

Boonsiriseth, A., R. M. Thorne, G. Lu, V. K. Jordanova, M. F. Thomsen, D. M. Ober, and A. J. Ridley (2001), A semiempirical equatorial mapping of AMIE convection electric potentials (MACEP) for the January 10, 1997, magnetic storm, *J. Geophys. Res.*, 106, 12,903.

Boyle, C. B., P. H. Reiff, and M. R. Hairston (1997), Empirical polar cap potentials, *J. Geophys. Res.*, 102, 111−125.

Burch, J. L. (2000), IMAGE mission overview, *Space Sci. Rev.*, 91, 1.

Chen, A. J. (1970), Penetration of low-energy protons deep into the magnetosphere, *J. Geophys. Res.*, 75, 2458.

Chen, M. W., M. Schulz, G. Lu, and L. R. Lyons (2003), Quasi-steady drift paths in a model magnetosphere with AMIE electric field: Implications for ring current formation, *J. Geophys. Res.*, 108(A5), 1180, doi:10.1029/2002JA009584.

Crooker, N. U., and G. L. Siscoe (1981), Birkeland currents as the cause of the low-altitude asymmetric disturbance field, *J. Geophys. Res.*, 86, 11,201.

C:son Brandt, P., Y. Ebihara, S. Barabash, and E. C. Roelof (2002a), Energetic neutral atom images of a narrow flow channel from the plasma sheet: Astrid-1 observations, *J. Geophys. Res.*, 107(A10), 1273, doi:10.1029/2001JA000230.

C:son Brandt, P., S. Ohtani, D. G. Mitchell, M.-C. Fok, E. C. Roelof, and R. Demajistre (2002b), Global ENA observations of the storm mainphase ring current: Implications for skewed electric fields in the inner magnetosphere, *Geophys. Res. Lett.*, 29(20), 1954, doi:10.1029/2002GL015160.

De Michelis, P., I. A. Daglis, and G. Consolini (1999), An average image of proton plasma pressure and of current systems in the equatorial plane derived from AMPTE/CCE-CHEM measurements, *J. Geophys. Res.*, 104, 28,615.

Ebihara, Y., and M. Ejiri (2000), Simulation study on fundamental properties of the storm-time ring current, *J. Geophys. Res.*, 105, 15,843.

Ebihara, Y., M. Ejiri, H. Nilsson, I. Sandahl, A. Milillo, M. Grande, J. F. Fennell, and J. L. Roeder (2002), Statistical distribution of the storm-time proton ring current: POLAR measurements, *Geophys. Res. Lett.*, 29(20), 1969, doi:10.1029/2002GL015430.

Ebihara, Y., M. Ejiri, H. Nilsson, I. Sandahl, M. Grande, J. F. Fennell, J. L. Roeder, D. R. Weimer, and T. A. Fritz (2004), Multiple discrete-energy ion features in the inner magnetosphere: February 9, 1998, event, *Ann. Geophys.*, 22, 1297.

Ejiri, M. (1978), Trajectory traces of charged particles in the magnetosphere, *J. Geophys. Res.*, 83, 4798.

Ejiri, M., R. A. Hoffman, and P. H. Smith (1980), Energetic particle penetrations into the inner magnetosphere, *J. Geophys. Res.*, 85, 653.

Fok, M.-C., and T. E. Moore (1997), Ring current modeling in a realistic magnetic field configuration, *Geophys. Res. Lett.*, 24, 1775.

Fok, M.-C., R. A. Wolf, R. W. Spiro, and T. E. Moore (2001), Comprehensive computational model of Earth's ring current, *J. Geophys. Res.*, 106, 8417.

Fok, M.-C., et al. (2003), Global ENA image simulations, *Space Sci. Rev.*, 109, 77.

Garner, T. W. (2003), Numerical experiments on the inner magnetospheric electric field, *J. Geophys. Res.*, 108(A10), 1373, doi:10.1029/2003JA010039.

Hardy, D. A., M. S. Gussenhoven, and E. Holeman (1985), A statistical model of auroral electron precipitation, *J. Geophys. Res.*, 90, 4229.

Hardy, D. A., M. S. Gussenhoven, R. Raistrick, and W. J. McNeil (1987), Statistical and functional representations of the pattern of auroral energy flux, number flux, and conductivity, *J. Geophys. Res.*, 92, 12,275.

Harel, M., R. A. Wolf, P. H. Reiff, R. W. Spiro, W. J. Burke, F. J. Rich, and M. Smiddy (1981), Quantitative simulation of a magnetospheric substorm: 1. Model logic and overview, *J. Geophys. Res.*, 86, 2217.

Hedin, A. E. (1991), Extension of the MSIS thermospheric model into the middle and lower atmosphere, *J. Geophys. Res.*, 96, 1159.

Hill, T. W., A. J. Dessler, and R. A. Wolf (1976), Mercury and Mars: The role of ionospheric conductivity in the acceleration of magnetospheric particles, *Geophys. Res. Lett.*, 3, 429.

Jaggi, R. K., and R. A. Wolf (1973), Self-consistent calculation of the motion of a sheet of ions in the magnetosphere, *J. Geophys. Res.*, 78, 2852.

Jordanova, V. K., J. U. Kozyra, A. F. Nagy, and G. V. Khazanov (1997), Kinetic model of the ring current-atmosphere interactions, *J. Geophys. Res.*, 102, 14,279.

Jordanova, V. K., C. J. Farrugia, J. M. Quinn, R. B. Torbert, J. E. Borovsky, R. B. Sheldon, and W. K. Peterson (1999), Simulation of off-equatorial ring current ion spectra measured by Polar for a moderate storm at solar minimum, *J. Geophys. Res.*, 104, 429.

Khazanov, G. V., M. W. Liemohn, T. S. Newman, M.-C. Fok, and R. W. Spiro (2003a), Self-consistent magnetosphere-ionosphere coupling: Theoretical studies, *J. Geophys. Res.*, 108(A3), 1122, doi:10.1029/2002JA009624.

Khazanov, G. V., K. V. Gamayunov, and V. K. Jordanova (2003b), Self-consistent model of magnetospheric ring current and electromagnetic ion cyclotron waves: The 2−7 May 1998 storm, *J. Geophys. Res.*, 108(A12), 1419, doi:10.1029/2003JA009856.

Khurana, K. K., R. J. Walker, and T. Ogino (1996), Magnetospheric convection in the presence of interplanetary magnetic field By: A conceptual model and simulations, *J. Geophys. Res.*, 101, 4907.

Lui, A. T. Y. (2003), Inner magnetospheric plasma pressure distribution and its local time asymmetry, *Geophys. Res. Lett.*, 30(16), 1846, doi:10.1029/2003GL017596.

Mitchell, D. G., et al. (2000), High energy neutral atom (HENA) imager for the IMAGE mission, *Space Sci. Rev.*, 91, 67.

Ober, D. M., N. C. Maynard, and W. J. Burke (2003), Testing the Hill model of transpolar potential saturation, *J. Geophys. Res.*, 108(A12), 1467, doi:10.1029/2003JA010154.

Rairden, R. L., L. A. Frank, and J. D. Craven (1986), Geocoronal imaging with Dynamics Explorer, *J. Geophys. Res.*, 91, 13,613.

Ridley, A. J., and M. W. Liemohn (2002), A model-derived storm time asymmetric ring current driven electric field description, *J. Geophys. Res.*, 107(A8), 1151, doi:10.1029/2001JA000051.

Sheldon, R. B., and D. C. Hamilton (1993), Ion transport and loss in the Earth's quiet ring current: 1. Data and standard model, *J. Geophys. Res.*, 98, 13,491.

Stancil, P. C., D. R. Schultz, M. Kimura, J.-P. Gu, G. Hirsch, and R. J. Buenker (1999), Charge transfer in collisions of O+ with H and H+ with O, *Astron. Astrophys. Suppl. Ser.*, 140, 225.

Stern, D. P. (1975), The motion of a proton in the equatorial magnetosphere, *J. Geophys. Res.*, 80, 595.

Stüdemann, W., et al. (1987), The May 2−3, 1986 magnetic storm: first energetic ion composition observations with the MICS instrument on Viking, *Geophys. Res. Lett.*, 14, 455.

Toffoletto, F., S. Sazykin, R. Spiro, and R. Wolf (2003), Inner magnetospheric modeling with the Rice Convection Model, *Space Sci. Rev.*, 107, 175.

Tsyganenko, N. A. (1995), Modeling the Earth's magnetospheric magnetic field confined within a realistic magnetopause, *J. Geophys. Res.*, 100(4), 5599.

Tsyganenko, N. A., and D. P. Stern (1996), A new-generation global magnetosphere field model, based on spacecraft magnetometer data, *ISTP Newsl.*, 6(1), 21.

Volland, H. (1973), A semiempirical model of large-scale magnetospheric electric fields, *J. Geophys. Res.*, 78, 171.

Weimer, D. R. (2001), An improved model of ionospheric electric potentials including substorm perturbations and application to the Geospace Environment Modeling November 24, 1996, event, *J. Geophys. Res.*, 106, 407.

Wolf, R. A. (1970), Effects of ionospheric conductivity on convection flow of plasma in the magnetosphere, *J. Geophys. Res.*, 75, 4677.

Wolf, R. A. (1983), The quasi-static (slow-flow) region of the magnetosphere, in *Solar Terrestrial Physics*, edited by R. L. Carovillano and J. M. Forbes, p. 303, D. Reidel, Norwell, Mass.

————————————
Y. Ebihara, National Institute of Polar Research, 1-9-10 Kaga, Itabashi-ku, Tokyo 173-8515, Japan. (ebihara@nipr.ac.jp)

M.-C. Fok, NASA Goddard Space Flight Center, Code 692, Greenbelt, MD 20771, USA. (mei-ching.h.fok@nasa.gov)